VIRULENCE
2026, VOL. 17, NO. 1, 2675087
https://doi.org/10.1080/21505594.2026.2675087

Taylor & Francis
by informa

HOST RESPONSE

OPEN ACCESS Check for updates

Single-cell spatial immune landscape of ASFV-infected porcine lung microenvironment

Hui Guo[a,b*], Huaiyuan Cai[a,b*], Yu Chen[a,c], Zhong Zou[b], Shengjie Yin[a,b], Yangyang Xu[a,b], Guiqing Peng[a,b], Meilin Jin [a,b], Gang Cao[a,b,d], and Jinxia Dai [a,b]

[a]State Key Laboratory of Agricultural Microbiology, Huazhong Agricultural University, Wuhan, China; [b]College of Veterinary Medicine, Huazhong Agricultural University, Wuhan, China; [c]College of Life Science and Technology, Huazhong Agricultural University, Wuhan, China; [d]Shenzhen Institute of Advanced Technology, Chinese Academy of Sciences, Shenzhen, China

ABSTRACT

African swine fever virus (ASFV) infection leads to severe lung lesions in the host, yet detailed insights into the *in vivo* immune response of the lung microenvironment to ASFV infection at the single-cell level remain limited. Here, we mapped the spatial immune landscape of the porcine lung microenvironment upon ASFV infection at single-cell resolution using an *in situ* multi-gene mRNA co-detection method. We delineated the transcriptional dynamics of candidate genes in different immune cell types within the pig lungs upon ASFV infection. Additionally, we observed the dynamic changes in the number and spatial distribution of specific immune cell types in the lung microenvironment during ASFV infection. Moreover, the expression correlation between viral multi-gene family genes and host genes related to antiviral responses and apoptosis was identified. Our findings highlight the impact of viral genes on the host lung microenvironment and the complex viral-host interactions, providing insights into ASFV immune responses in porcine lungs at an *in vivo* level.

SUMMARY

Importance African swine fever caused by African swine fever virus (ASFV) brought huge economic losses to the global swine industry. Many studies on the mechanism of ASFV infection and host response were carried out. However, the *in vivo* and *in situ* landscape of host response to ASFV infection in heterogeneous microenvironments remains to be elucidated. We delineated the spatial transcriptome dynamics of key functional genes from both host and ASFV in pig lungs upon ASFV infection at single-cell resolution, including transcriptomic dynamics of different cell types, spatial location changes of certain cells, and the genes-expression correlation between host and ASFV. Our work provided valuable information for immune dynamics of host lung microenvironment as ASFV infection, helping for understanding ASFV-host interaction and ASFV pathology.

ARTICLE HISTORY
Received 23 April 2025
Revised 18 November 2025
Accepted 10 May 2026

KEYWORDS
African swine fever virus; spatial transcriptomics; lung microenvironment; single-cell resolution; *in vivo*

Introduction

African swine fever (ASF), caused by African swine fever virus (ASFV), is a highly contagious and fatal disease that has led to significant economic losses in the global swine industry [1–3]. ASF is characterized by high fever and hemorrhagic lesions in multiple organs of swine, including the lungs [4,5]. The severe pathological lesions in porcine lungs (hemorrhage, inflammatory infiltration, edema) caused by ASFV infection lead to respiratory distress, which contributes to the mortality of infected pigs [6]. As an important target organ of ASFV, the lungs are rich in immune cells. In porcine lungs, ASFV infection induces infiltration of inflammatory cells, overproduction of cytokines, and dysfunction of immune cells [7,8], all of which are closely related to the dynamic regulation of immune microenvironment. This makes porcine lungs an ideal model for investigating the pathogenic mechanisms underlying ASFV infection. Many studies on the mechanisms of ASFV infection and host cell response have been performed *ex vivo* in macrophages, such as porcine alveolar macrophages (PAMs) [9–13]. The *in vivo* immune responses in porcine lungs following ASFV infection, beyond alveolar macrophages, have yet to be fully delineated. Elucidating the detailed changes in the microenvironment of porcine lungs, including the transcriptomic dynamics of different cell types and spatial alterations in

CONTACT Jinxia Dai jxdai@mail.hzau.edu.cn
*These authors contributed equally.
Supplemental data for this article can be accessed online at https://doi.org/10.1080/21505594.2026.2675087

cell distribution upon ASFV infection, will deepen our understanding on ASF pathology.

High-throughput transcriptome sequencing (RNA-seq and single-cell RNA-seq) analyses reveal that ASFV infection significantly alters gene expression profiles of host cells [11,14,15]. The IFN-stimulated gene *MX1*, central transcription factor gene *STAT1*, and genes associated with NF-κB signaling pathway activation (such as *TNFA* and *TNFAIP3*) were significantly up-regulated in ASFV-infected PAMs [11,14,16,17]. Some genes, such as *DUSP1*, which inhibits viral replication, were down-regulated [11,18]. ASFV utilizes endoplasmic reticulum (ER) as a key site for replication, triggering ER stress and the unfolded protein response (UPR) [19]. Accordingly, UPR-associated genes (*DDIT3*, *PIK3R1*), energy metabolism gene (*COX1*), and transcription-related genes (*RPS7*) were up-regulated, promoting viral replication and persistent infection [11]. *TMEM107*, a gene for cilia development and regulation, was also up-regulated, potentially facilitating viral infection and transmission [11,20,21]. ASFV modulated the expression of TNF family genes (*TNFSF10* and *TNFSF13B*) to promote viral replication and persistent infection [14]. ASFV infection also caused up-regulation of pro-inflammatory cytokines (*IL17A* and *IFN*) and down-regulation of anti-inflammatory cytokines (*IL10* and *TGF-β*) [15,22]. Moreover, ASFV may prolong viral infection by reducing the expression of chemokine genes (*CSF3*, *IL8*, *CXCL10*) required for the recruitment of neutrophils or CD8 T cells [22–24].

ASFV genes exhibit distinct expression patterns and functions to facilitate viral replication and immune evasion. Multiple ASFV genes in MGF 110 and MGF 360 families were highly expressed during infection at multiple time points [11]. MGF 360-9 L suppresses IFN-β signaling, helping ASFV evade host immune response [25]. MGF 505-7 R strongly inhibits IL-1β maturation and IFN-β activation [26]. Additionally, MGF 110-9 L suppresses type I interferon expression and cellular antiviral responses [27]. The structural protein CD2v, encoded by *EP402R*, is an important virulent protein of ASFV [28]. And *EP402R* is highly expressed at all time points of infection in macrophages [11]. *S273R*, expressed at late stage of infection, inhibits cell apoptosis and represses cGAS-STING pathway-mediated type I interferon production [29]. Meanwhile, the major capsid protein P72, abundant at late stage of infection, facilitates viral entry by binding to CD1D on PAMs [11,30]. Collectively, these findings highlight a dynamic interplay between ASFV and host cells, where viral gene expression strategically manipulates immune defenses and cellular processes to sustain infection.

In this study, leveraging published RNA-sequencing data, we selected key genes of host and ASFV to delineate their spatial transcriptomic landscape in porcine lung microenvironment upon ASFV infection at single-cell resolution. Spatial transcriptomic analysis has proven essential for revealing the architecture and interactions of immune cells within complex tissues, and it is increasingly integrated with immunological profiling in medical research focused on immune landscape mapping [31–33]. Our analysis revealed significant alterations in host gene expression linked to antiviral response, inflammatory signaling, apoptosis, and metabolic regulation. Concurrently, several viral genes also exhibited dynamic expression patterns, underscoring the impact of viral genes on the host microenvironment and the intricate interactions between ASFV and host cells. Furthermore, we uncovered changes in immune cell numbers and spatial relationships. Our data provide valuable insights into the changes in pig lung microenvironment during ASFV infection, which will aid in exploring the mechanisms of ASFV-host interactions and the pathology of ASF.

Results

Gradually intensified virus dissemination in pigs after oral infection of ASFV

Based on previous *ex vivo* studies of host cell transcriptomic responses to ASFV infection and the existing single-cell atlas of porcine lungs [11,15,34], we selected 50 genes to investigate the single-cell spatial immune landscape of porcine lung microenvironments upon ASFV infection. The selection comprised 43 host genes (including 16 cell-marker genes, 25 differentially expressed genes (DEGs) in ASFV-infected PAMs, plus *PD-1* and *PD-L1* genes) and 7 viral genes (*MGF 505-7 R*, *MGF 110-9 L*, *MGF 360-9 L*, *MGF 360-2 L*, *B646L*, *S273R*, *EP402R*) (Table S1). The 25 host DEGs include genes related to metabolism, transcription regulation, antiviral responses, and apoptosis. Given the important role of PD-1 and PD-L1 in the pulmonary immune microenvironment [35,36], their expression was also examined. ASFV gene candidates were primarily key genes involved in immunosuppression and anti-apoptosis [37].

The main transmission routes of ASFV consist of ingestion of contaminated feed and direct contact with infected swine [38–40]. To simulate a natural ASFV infection, piglets were orally challenged with the ASFV SY-1 strain, a highly virulent strain belonging

to genotype II ASFV, at a dose of 2×10^2 HAD_{50} (Figure 1(A)). Meanwhile, for transcriptomic dynamics analysis, tissues were collected at two time points: (1) 11 days post infection (dpi), representing the early infection stage when the challenged piglets exhibited persistent fever (>40°C) and the viral load was approximately 10 copies of p72/mL, and (2) 23 dpi, representing the late stage infection with high viral load (approaching 10^3 copies of p72/mL) (Figure 1(B–E) and Figure S1A-1D). *In situ* codetection of 50 genes transcripts was performed on the same paraffin section, and the spatial expression of genes at single-cell resolution was compared between ASFV-challenged and mock-treated samples at both time points (Figure 1(A)).

Following infection, the onset of rectal temperature elevation in ASFV-challenged pigs coincided with the initial detection of viral DNA in swab samples (Figure 1 (B–E) and Figure S1A-1D). Both rectal temperature and viral load in challenged pigs gradually increased over time (Figure 1(B–E) and Figure S1A-1D). In the early sample group, one pig with high fever (maximum 42.3°C) and high viral load died at 11 dpi and was excluded from analysis (Figure 1(B,D) and Figure S1A, 1C). Gross lesions characterized by extensive hemorrhaging in multiple organs (lung, liver, and spleen) were worsened with infection progression (Figure S1E). Pathological changes in ASFV-challenged pig lungs were manifested as focal hemorrhages with mild inflammatory cell infiltration in early samples, and extensive hemorrhage with massive inflammatory cell infiltration in late samples (Figure 1(F)).

Overall spatial transcriptomic dynamics in pig lung microenvironment upon ASFV infection

The spatial transcriptomic profiles of 50 genes in lung slices from both early and late samples are visualized in Figures 1(G–H). After cell segmentation and gene assignment, mRNA signals were analyzed at single-cell resolution. Among 27 host genes (25 DEGs, *PD-1*, and *PD-L1*), with the exception of *IL8*, which showed no significant alteration, five distinct patterns of gene expression change were observed. Sustained up-regulation was detected for *MX1*, *STAT1*, *PYCARD*, and *CCL2* during ASFV infection (Figure 1(I) and Figure S2A). In contrast, twelve genes (*DUSP1*, *TNFA*, *TMEM107*, *COX1*, *IFNA*, *IFNB*, *IL10*, *TGFB*, *TNFSF10*, *TNFSF13B*, *CSF3*, *CD279*) exhibited persistent down-regulation (Figure 1(I) and Figure S2A). *PIK3R1* expression increased initially but decreased at the late stage of infection, whereas *RPS7*, *CD1D*, *DDIT3*, *TNFAIP3*, *IFNG*, *IL17A*, and *IL1B2* genes showed opposite expression patterns from early to late infection stage (Figure S2A). Lastly, expression changes at either early or late infection stage were observed for *PD-L1* and *CXCL10*, with *PD-L1* expression being reduced at the early stage and *CXCL10* being down-regulated at the late stage (Figure S2A).

All seven viral genes were detected in both early and late samples of ASFV-infected lungs. Of these, *B646L* and *MGF 360-2 L* showed stable expression (Figure 1(J) and Figure S2B). In contrast, the remaining five genes exhibited expression changes from early to late stages, as indicated by decreased expression of *MGF 360-9 L* and *MGF 505-7 R*, and increased expression of *MGF 110-9 L*, *S273R*, and *EP402R* (Figure 1(J) and Figure S2B). As interferon inhibitors, *MGF 360-9 L* and *MGF 505-7 R* were highly expressed early and play important roles in immune evasion [11,14]. The higher levels of *MGF 360-9 L* and *MGF 505-7 R* expression in early infected samples we detected are consistent with their functions during the initial infection phase. The higher levels of *S273R* and *EP402R* expression in the late samples also align with their primary functions in the late phase of viral replication [11,29].

Cellular composition changes in pig lung microenvironment upon ASFV infection

Based on cell-marker genes expression, fifteen major cell types in pig lungs, including structural cells and immune cells, were annotated (Figure 2(A–B)). The remaining cells without significant expression of marker genes, were categorized as undefined cells (Figure 2 (A–B)). These cells were clearly annotated in lung slices (Figure 2(C) and Figure S3-4). The proportions of each cell type across all images are shown in Figure 2(D). Cell clustering analysis revealed similar cell clustering patterns of images from different lung lobes, indicating the slices from different lobes were comparable (Figure S3A). No significant differences in the total cell counts for each image were observed between infected and control samples (Figure 2(E)). However, the degree of cell dispersion was significantly greater in the pulmonary microenvironment of ASFV-infected pig lungs at the late stage, as indicated by significantly lower Moran's I values (Figure 2(F)). This suggests that ASFV infection induces a more random distribution of cells in the lung microenvironment, with a loss of defined structural organization.

Although no significant changes were observed in the total cell count of porcine lung microenvironment under ASFV infection, certain immune cell types exhibited cell number alteration. The proportion of dendritic

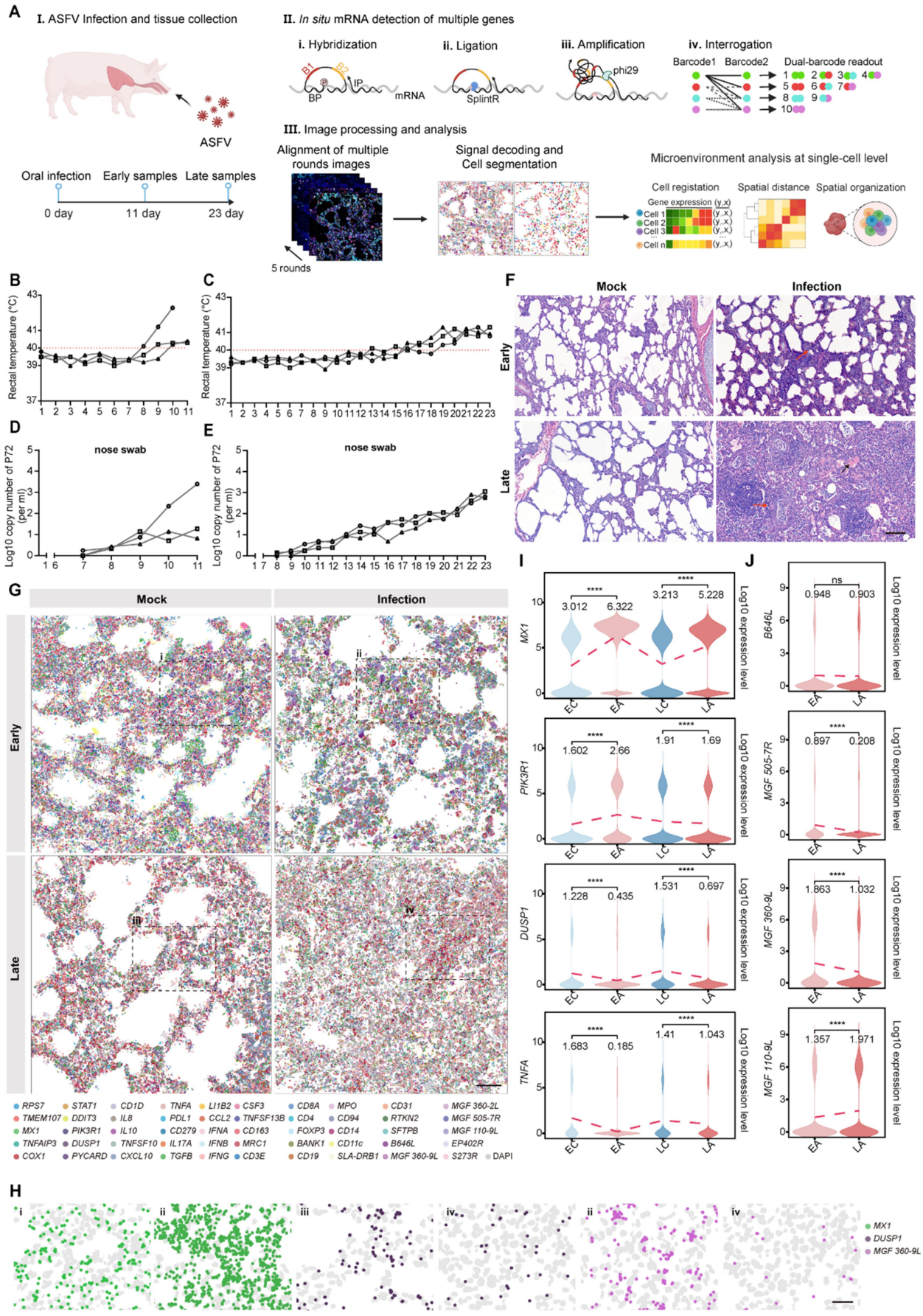

Figure 1. Spatial transcriptomic mapping of pig lung microenvironment upon ASFV infection via *in situ* multi-genes mRNA co-detection.(A) Schematic diagram of experimental workflow. Images were created with BioRender.com. BP, barcoded probe; B1,

cells was significantly increased, while that of neutrophils decreased in the early samples of ASFV-infected pig lungs compared to mock controls (Figure 2(G)). At the late infection stage, the ratio of natural killer (NK) cells was higher, but that of T helper (Th) cells was lower compared to mock controls (Figure 2(H)). Further comparison of cell proportions between early and late infected samples revealed that the proportions of B cells and neutrophils were significantly elevated at the late stage (Figure 2(I)). In contrast, the proportions of alveolar macrophages and cytotoxic T cell (Tc) were lower in the late-infected samples compared to the early-infected samples (Figure 2(I)).

No differences were observed in ASFV-infected cell number between early and late stages (Figure 2(J)). ASFV infected all annotated cell types, primarily targeting macrophages (Mac) and alveolar macrophages (AM) (Figure 2(K)). Co-detection of viral P72 protein and marker genes mRNA for B cells (*CD19*), NK cells (*CD94*), and neutrophils (*MPO*) confirmed the infection to these cells besides Mac and AM (Figure S5A). From early to late stage, the proportion of infected Mac decreased, while that of infected neutrophils, T helper cells (Th), and undefined cells increased (Figure 2(K)).

Since ASFV infection causes apoptosis of immune cells in peripheral blood and various tissues [12,41–43], we further investigated cell apoptosis in pig lungs upon infection. Widespread apoptosis was detected in both early and late-infected samples, with exacerbation at the late stage (Figure S5B-5C). Cell apoptosis occurred in all annotated cell types and dramatically increased at the late stage in most cell types (Figure S5D). Notably, undefined cells at the late stage accounted for the highest percentage of all apoptotic cells (Figure S5E-5F).

Spatial location changes of certain immune cell types in pig lung microenvironment

To further explore the changes in the pig lung microenvironment upon ASFV infection, we analyzed the spatial interrelationship among different cell types. Based on mean hop distance analysis, we found both natural killer (NK) cells and dendritic cells became closer to other cell types (Figure 3(A)). These spatial alterations may be partially attributed to corresponding changes in cell numbers. Increased numbers of NK cells and dendritic cells (Figure 2(G–I)) likely contributed to their closer proximity to other cell types.

It is noteworthy that B cells and neutrophils exhibited significantly increased intercellular distances at the early stage of infection (Figure 3(A)). After excluding the effect of cell number changes, we separately measured the spatial distance from each B cell to all surrounding neutrophils, and from each neutrophil to all surrounding B cells. Both analyses consistently demonstrated significantly increased distance between B cells and neutrophils at the early stage of infection (Figure 3(B–C)). However, at the late stage of infection, this distance decreased, becoming notably closer (Figure 3(D–E)). Furthermore, the spatial distance between B cells and neutrophils was significantly reduced at the late stage compared to the early stage of infection (Figure S6A-6B). This temporal dynamic alteration in B cells-neutrophils spatial distance was clearly evident in pig lung tissue slices (Figure 3(F)).

Intercellular distances analysis after stratifying cell types into ASFV-infected (positive, P) and bystander (negative, N) cells revealed that NK cell-P maintained greater distances from other cell types throughout both infection stages, while NK cell-N became closer to other cells from early to late stage. Therefore, the closer distance of NK cells to other cell types (Figure 3(A)) may be primarily attributed by NK bystander cells. The distances of Neutrophil-N and B cell-N to other cell types were greater at the early stage but closer at the late stage of infection (Figure S6C), which could explain the increased distance of B cells and neutrophils from other cells at the early stage (Figure 3(A)). Both infected and non-infected alveolar macrophages (AM) became farther away from other cell types from early to late stage of infection (Figure S6C), contributing to the greater distance of AM cells from other cell types at the late stage of infection (Figure 3(A)).

barcode 1; B2, barcode 2; IP, initiator primer probe. (B-C) Rectal temperature changes of pigs in early (b) and late (C) infection groups. The dashed line indicated 40°C. (D-E) Viral loads detected in nose swabs. (F) HE staining images for the histopathological characteristics of pig lungs under ASFV infection. Red arrows indicate the inflammatory cell infiltration. Black arrow indicates hemorrhage. (G) Spatial transcriptome of 50 genes in slices from normal and ASFV-infected pig lung tissues. (H) Spatial pattern of genes transcripts for *MX1*, *DUSP1*, and *MGF 360-9 L* in the rectangle areas (i, ii, iii, iv) in G. (I) Violin plots of gene expression level for *MX1*, *PIK3R1*, *DUSP1*, and *TNFA* in cells of pig lung tissue slices. (J) Violin plots of expression levels for viral genes (*B646L*, *MGF 360-9 L*, *MGF 505-7 R*, *MGF 110-9 L*) in cells of pig lung tissue slices. Statistical significance was assessed through Student's t-test (two-tailed). The numbers in I and J represent the median. ns: $p>0.05$, *$p < 0.05$, **$p < 0.01$, ***$p < 0.001$, ****: $p < 0.0001$. EC, early samples of mock controls; LC, late samples of mock controls; EA, early samples of ASFV infection; LA, late samples of ASFV infection. Scale bars, 20 μm in F, 50 μm in G, 25 μm in H.

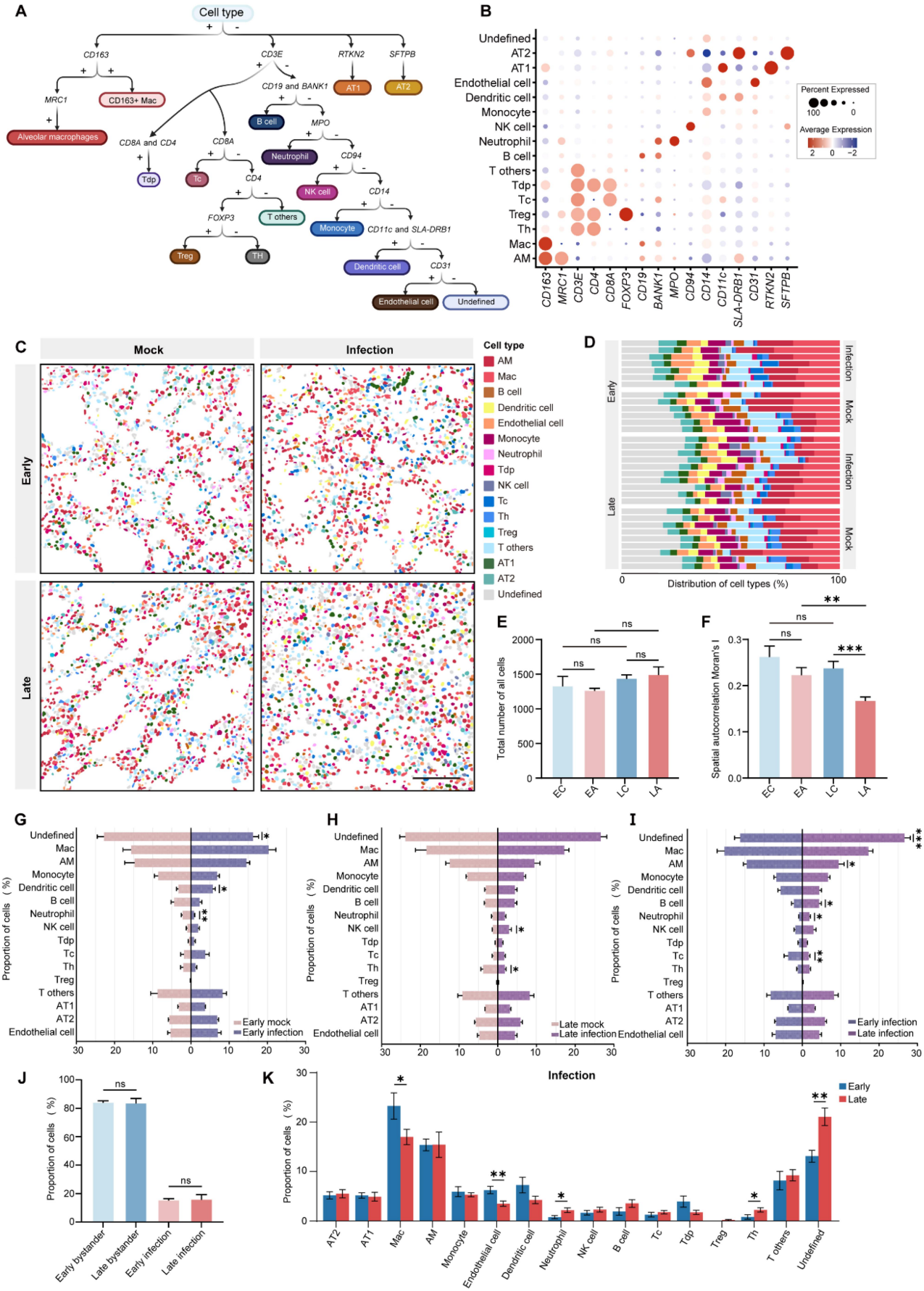

Figure 2. Cell number change in pig lung tissues upon ASFV infection.(A) Schematic description of marker genes for cell type identification in pig lungs. Images were created with BioRender.com. (B) Average expression of marker genes in different cell types.

To investigate the effect of viral load on cell distribution, infected cells were divided into three viral-load states based on *B646L* mRNA signal counts: semi (counts ≤ 9), high (9 < counts ≤27), and high+ (counts > 27) (Figure 3(G)). The percentage of semi-viral-load cells increased, while that of high-viral-load cells decreased in late samples compared to early samples (Figure S6D). From early to late stage, high-viral-load states (high and high+) expanded from being present in most cell types to encompassing all cell types (Figure 3 (H–I)). Cell apoptosis in three viral-load states did not significantly increase at the late stage, although an increased tendency was observed (Figure S6E). Nonetheless, apoptotic cells were mainly derived from bystander cells, with a lesser contribution from semi-viral-load cells (Figure S6F). In the spleen, monocytes exhibit the most extensive viral-load status upon ASFV infection [20]. Our co-detection of cell marker genes and *B646L* transcripts in pig spleens (Figure S6G) confirmed the high infection tendency and viral load in splenic monocytes (Figure S6H-6I), further validating the reliability of viral-load results in pig lungs. Based on the mean hop distance, we found high+ cells became more distant from the other three cell populations (high, semi, and bystanders) at the late stage compared to the early stage (Figure 3(J)). High cells showed greater distances to all types of cells at the late stage than at the early stage (Figure S6J). Furthermore, the spatial pattern of ASFV infection in the microenvironment of pig lungs shifted from aggregated to more dispersed infection (Figure 3(K)).

Changes in cell distribution and transcriptome around high-infection centers

To further assess ASFV's impact on the immune microenvironment of pig lungs, we selected high-infection centers based on viral load to analyze changes in cell distribution and transcriptome in the surrounding areas. For each image, five high-infection centers were identified, with surrounding areas divided into inner (0–60 pixels), middle (60–120 pixels), and outer (120-–180 pixels) layers (Figure 4(A–B)). At the early stage, the inner layer exhibited a higher proportion of dendritic cells but lower proportions of neutrophils and Th cells, indicating dendritic cell clustering near high-infection centers while neutrophils and Th cells remained distally localized (Figure 4(C)). The higher proportion of dendritic cells in the inner layer may help initiate adaptive immune responses toward the infection center. At the late stage, the proportion of AM was significantly higher in the inner layers (Figure 4(D)), indicating AM was closer to the high-infection center.

We then analyzed transcriptomic changes surrounding high-infection centers (Figure 4(E) and Figure S7-8). The expression of ASFV *B646L* from inner to outer layers was shown in Figure 4(F). *STAT1* and apoptosis-related genes (including *DDIT3* and *PIK3R1*) showed increasing expression from inner to outer layers at the late stage, indicating a negative correlation with viral load (Figure 4(G) and Figure S7-8). Notably, *DUSP1*, a gene that inhibits viral replication [20], also showed higher expression in outer layers, further suggesting a negative correlation with viral load (Figure 4(H)). Additionally, cytokine genes exhibited differential expression changes (Figure S7-8). For instance, the expression of chemokines for neutrophil recruitment (such as *IL8*) increased from inner to outer layers at the early stage (Figure S7), aligning with neutrophils distribution trend (Figure 4(C)).

Host-ASFV genes expression correlation in certain cell types

The expression correlation between host gene and viral gene in the microenvironment of pig lungs was further explored to reveal the characteristics of different cell types in response to viral infection. Firstly, the expression dynamics of 27 host genes (25 DEGs, *PD-1*, and *PD-L1*) in different cell types upon ASFV infection were analyzed. Notably, *MX1* and *STAT1* were significantly up-regulated in all cell types at the early stage of

AT1, alveolar type I epithelial cells; AT2, alveolar type II epithelial cells; AM, alveolar macrophages; Mac, macrophage; NK, natural killer; Tdp, double positive T cell; Tc, cytotoxic T cell; Th, helper T cell; Treg, regulatory T cells. (C) Images of annotated cell types indicated with distinct pseudo-colors. Scale bar, 100 μm. (D) Waterfall plots of cell proportion in pig lung tissue slices. The color representation is consistent with that in C. (E) Total cell number of each image for early and late samples. (F) the degree of cell dispersion. Higher values of Moran's I indicate more patterned distribution, whereas lower values indicate more random distribution. (G-H) Differences of cell proportion between infection and control samples. (I) Comparison of cell proportion between early and late samples of infection. (J) the percentage of bystander (uninfected) and ASFV-infected cells in the images of early and late samples. (K) Differential statistics of the percentage for infected cells between early and late samples for each cell type. Data was presented as mean ± SEM in E-K, and the statistical significance for E-K was measured by Student's t-test (two-tailed). ns: $p > 0.05$, *$p < 0.05$, **$p < 0.01$, ***$p < 0.001$. Sample size for E-K: $n = 6$ images for early mock; $n = 7$ images for early infection; $n = 9$ images for late mock; $n = 10$ image for late infection.

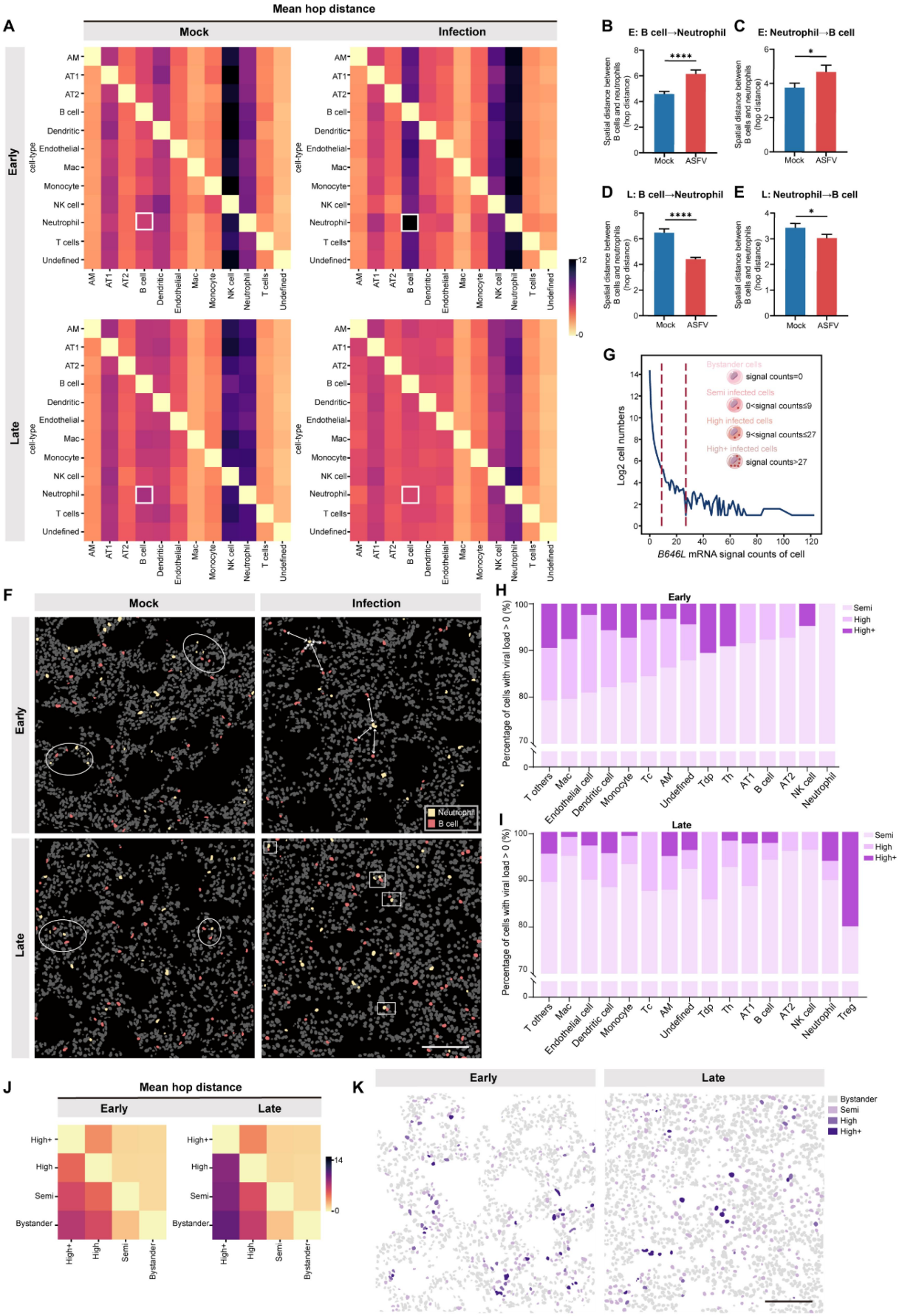

Figure 3. Spatial change of certain cell types in pig lung tissues upon ASFV infection.(A) Heatmap of mean hop distance among different types of cells in pig lung tissues from early and late samples. The white square box highlights the significant change of

infection compared to controls (Figure 5(A)). The increase in *MX1* expression was sustained in almost all cell-types through to the late stage, whereas *STAT1* up-regulation was maintained in certain cell types, including Th and Tc cells (Figure 5(A)). Concurrently, the up-regulation of both *MX1* and *STAT1* was partially attenuated as infection progressed (Figure 5(A) and Figure S9A), suggesting an initially robust antiviral response across all cell types that gradually diminished with persistent viral replication and dissemination.

Several genes, including *PIK3R1* and *CCL2*, were up-regulated in multiple cell types at certain stages of ASFV infection (Figure 5(A)). Conversely, multiple cytokine genes (*TNFA*, *TNFSF10*, *TNFSF13B*, *IL10*, *CSF3*) and PD-1 gene (*CD279*) were significantly down-regulated in most cell types at certain stages (Figure 5(A) and Figure S9A). The PD-1/PD-L1 checkpoint, a crucial regulator in tumor immunity, is exploited by viruses such as herpesviruses to evade host immune responses [35,36,44]. It is reported that ASFV-induced transcriptomic remodeling not only involves immune-related pathways but also extends to oncogene regulation [45]. The decreased expression of PD-1 gene *CD279* upon ASFV infection suggests a similar immune evasion strategy. Additionally, *IL1B2* expression decreased at the early stage but increased at the late stage in multiple cell types during ASFV infection (Figure 5(A) and Figure S9A). Genes such as *PYCARD*, *IL8*, *DDIT3*, and *IL17A* showed cell-type specific expression changes (Figure 5(A) and Figure S9A).

Next, we examined the expression profiles of 7 viral genes in different cell types at both infection stages. A high proportion of AT2 cells expressed *MGF 505-7 R* at the early stage, but fewer AT2 cells were detected with *MGF 505-7 R* expression at the late stage (Figure 5 (B–E)). Similarly, the expression of both *MGF 110-9 L* and *MGF 360-9 L* in macrophages (Mac) and *MGF 360-9 L* in neutrophils was reduced at the late stage compared to the early stage (Figure 5(B–E) and Figure S9B-9C). In contrast, the proportion of AM expressing *MGF 110-9 L* increased at the late stage compared to the early stage (Figure 5(B–E)).

A significant difference in the expression correlation between host genes and ASFV genes at different stages of infection was observed. The correlation between antiviral response-related genes (*MX1*, *STAT1*) and multiple cytokine genes (*IFNA*, *IFNB*, *IFNG*, *CSF3*) with viral multigene family (MGF) genes (*MGF 110-9 L*, *MGF 505-7 R*, *MGF 360-2 L*, *MGF 360-9 L*) underwent a dynamic change from strong at the early stage to weak at the late stage (Figure 5(F–I)). Similarly, the correlation between apoptosis-related genes (*TNFAIP3*, *DUSP1*, *PIK3R1*, *PYCARD*) and viral MGF genes also showed a significant change from strong to weak (Figure 5 (F–I)). However, the correlation of *TNFA*, *IL1B2*, *IL10*, and *IL17A* with viral MGF genes became stronger at the late stage (Figure 5(F)).

Discussion

Although many studies have been conducted on the mechanisms of ASFV infection, the understanding of its *in vivo* pathology and interaction with host remains limited. Therefore, delineating the *in vivo* landscape of ASFV infection, particularly the responses of different cell types (including transcriptomic dynamics and spatial changes in cell location) within the complex microenvironment of pig lungs, will undoubtedly help uncover the precise mechanisms of ASF pathology and ASFV-host interactions. To this end, we mapped the detailed spatial landscape of immune microenvironment in pig lungs upon ASFV infection at the *in vivo* levels with single-cell resolution, focusing on key genes identified from RNA-seq data of ASFV-infected alveolar macrophages (AMs). Future studies using single-cell RNA-seq data from ASFV-infected porcine lungs will provide a more comprehensive *in vivo* dynamic landscape.

Our results revealed complex transcriptomic dynamics of key genes in different cell types within pig lung microenvironment during ASFV infection.

mean hop distance between B cells and neutrophils. (B-E) Spatial distance between B cells and neutrophils at early and late stages. E, early; L, late. Early mock: $n = 6$ images; early infection: $n = 7$ images; late mock: $n = 9$ images; late infection: $n = 10$ image. Data was presented as mean ± SEM, and the statistical significance was measured by Student's t-test (two-tailed). *$p < 0.05$, **$p < 0.0001$. (F) Spatial distribution of B cells and neutrophils in the microenvironment of pig lung slices. Circles, double-arrowed lines, and rectangular boxes respectively indicate the distance between B cells and neutrophils in slices of control, early infection stage, and late infection stage. (G) Three viral-load states classified based on *B646L* mRNA signal counts according to the two inflection points (9 and 27) of kneed clustering algorithm. (H-I) Cell proportion of three viral-load states for each cell type. (J) Heatmap of mean hop distance among cells of three viral-load states and bystanders. (K) Spatial distribution of infected cells and bystanders in the microenvironment of pig lung slices. AT1, alveolar type I epithelial cells; AT2, alveolar type II epithelial cells; AM, alveolar macrophages; Mac, macrophage; NK, natural killer; Tdp, double positive T cell; Tc, cytotoxic T cell; Th, helper T cell; Treg, regulatory T cells. Scale bars, 100 μm in F and K.

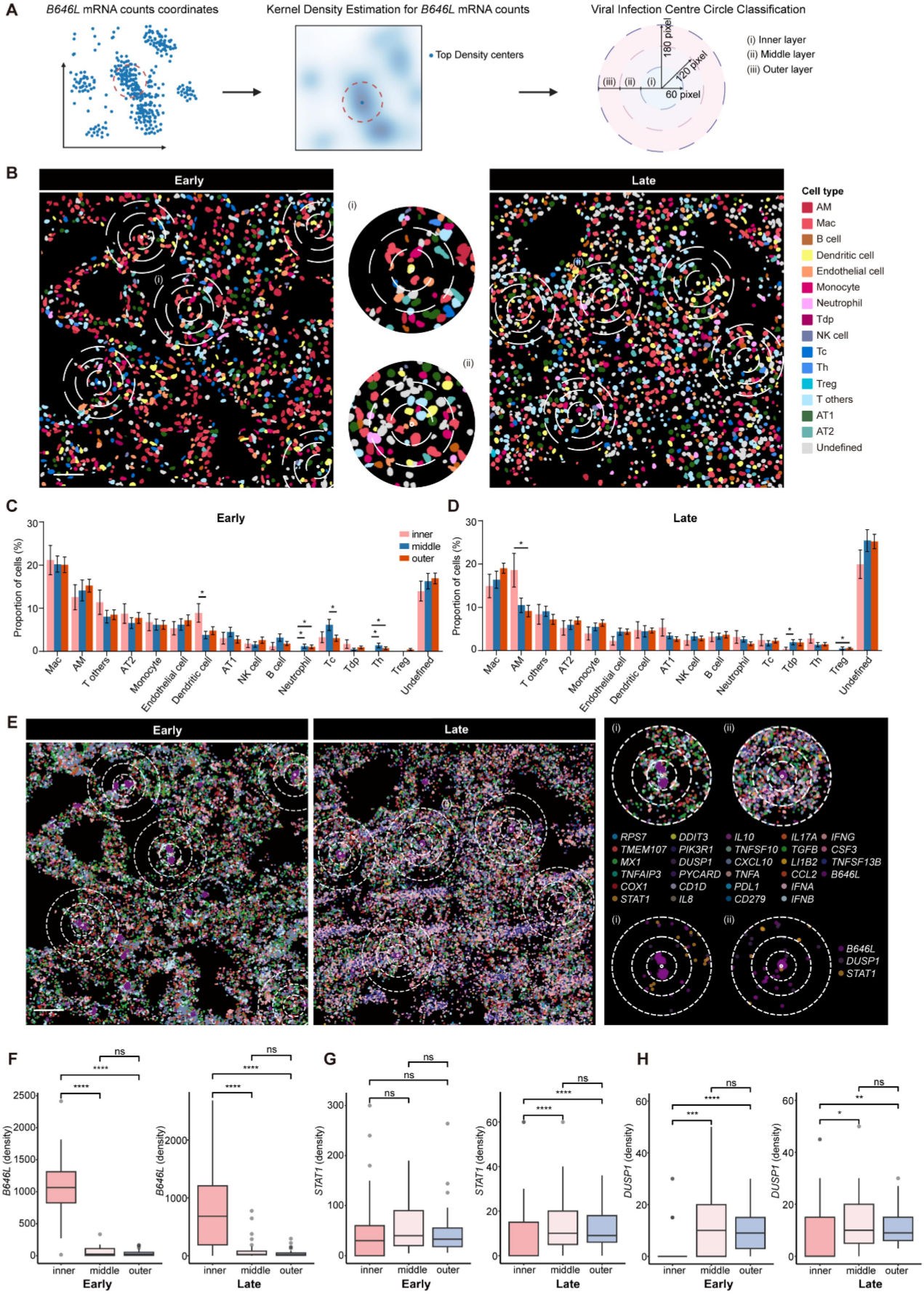

Figure 4. Changes of cell distribution and transcriptome around high-infection centers (A) Schematic illustration for the division of different circles from high viral infection center. Images were created with BioRender.com. 60 pixels ≈4.16 μm. (B) Cell distribution around

The sustained up-regulation of *MX1* and *STAT1* in all cell types indicated a broad antiviral response. STAT1, as a key molecule in the interferon signaling pathway, is an important regulator of the host's antiviral response [16]. During ASFV infection, the upregulation of inflammatory cytokines (including *TNFA*) is observed in porcine alveolar macrophages (PAMs) [11]. However, our study revealed downregulation of multiple cytokine genes (*TNFA*, *TNFSF10*, *TNFSF13B*, *IL10*, *IFNA*, *IFNB*, *IFNG*, *TGFB*) in multiple cell types of pig lungs at either or both infection stages. Interferons are key molecules in the antiviral immune response, capable of inducing an antiviral state, promoting immune cell activation and migration, and inhibiting viral replication [46], thereby facilitating efficient viral replication and dissemination within the host. Additionally, ASFV inhibits the expression of tumor necrosis factor-alpha (TNF-α), which is consistent with previous studies [11].

This observation may suggest that suppression of various inflammatory factors in host lungs during natural infection and ongoing disease progression could contribute to ASFV immune evasion, thereby facilitating viral replication and dissemination within the complex *in vivo* immune microenvironment. Although our study revealed dynamic changes in key genes at the transcriptional level, the protein expression or post-translational modifications of several critical genes (such as *MX1, STAT1, TNFA*, *et al.*) have not been validated. The expression and modifications of these key host and viral proteins may play crucial roles in immune evasion and the progression of infection. Therefore, future studies should also focus on protein-level validation to further establish the connection between transcriptional changes and protein function.

DUSP1, which inhibits ASFV replication [20], was persistently suppressed in pig lung microenvironment during ASFV infection, potentially disrupting host cell signaling pathways and inhibiting antiviral responses to promote ASFV replication and transmission in the lungs. Moreover, the increased expression of the unfolded protein response gene *DDIT3* and the mitochondrial apoptosis pathway gene *PYCARD* may induce apoptosis, which coincided with the exacerbated cell apoptosis observed during ASFV infection.

Several chemokines' genes (like *IL8*, *CCL2*) exhibited variable expression patterns across different cell types during ASFV infection. IL-8, secreted by macrophages and epithelial cells, primarily attracts neutrophils to infection sites, thereby initiating and sustaining inflammatory responses [47]. Down-regulation of *IL8* expression in macrophages at the early stage may inhibit neutrophil activation and migration. Conversely, upregulated *IL8* expression in both macrophages and alveolar type II epithelial cells at the late stage of infection may promote neutrophil aggregation to infected areas. *CCL2*, a chemokine for neutrophils, showed sustained upregulation across multiple cell types, which is consistent with recent findings [48].

In addition to transcriptomic dynamics, changes in cell numbers and spatial distribution of immune cells in pig lung microenvironment were also observed during ASFV infection. The increased number of dendritic cells at the early infection stage may be attributed to their migration to the lungs, bringing them spatially closer to other immune cells, which might increase the likelihood of their interactions and further contribute to the host's antiviral immune response [49,50]. At the late stage of infection, AM became spatially distant from other cell types, likely due to increased depletion or apoptosis of these cells [41]. The increased number of B cells at the late stage of ASFV infection is consistent with its adaptive immunity's role in antibody production. It is noteworthy that the spatial distance between B cells and neutrophils exhibits dynamic changes during ASFV infection, yet the underlying molecular mechanisms and biological functions remain unclear. In the early stages of ASFV infection, immune evasion mechanisms may delay the transmission of chemotactic signals (such as interleukin-8 (IL-8)), thereby inhibiting neutrophil migration to the site of infection. As the infection progresses and the host immune response strengthens, neutrophils gradually migrate to the infection site and cooperate with B cells to enhance local antiviral responses.

Moreover, our results indicated a broad infection capability of ASFV across all cell types in pig lungs. A recent study of the single-cell profiling in the spleens of ASFV infected pigs revealed that splenic T cells can be infected by ASFV *in vivo*, albeit at low frequency [20].

high-infection centers. Five high-infection centers were identified for each image. The cell distribution around high-infection centers from i and ii were zoomed-in the middle panel. (C-D) Percentage of cells in the three layers around high infection center at early (C) and late (D) stages of infection. (E) Spatial transcriptome around high-infection centers in images from early and late samples of ASFV infection. (i) and (ii) were zoomed-in the right-upper panel, and the three genes (*B646L*, *DUSP1*, *STAT1*) distribution in (i) and (ii) were presented in the right-lower panel. (F-H) Box-plots of expression density for *B646L* mRNA (F), *STAT1* mRNA (G), and *DUSP1* mRNA (H) in three layers around high-infection center at both early and late stages of infection. Statistical significance was assessed through Wilcoxon rank-sum test. ns: $p > 0.05$, *$p < 0.05$, **$p < 0.01$, ***$p < 0.001$, ****$p < 0.0001$. Scale bars, 50 μm in B and E.

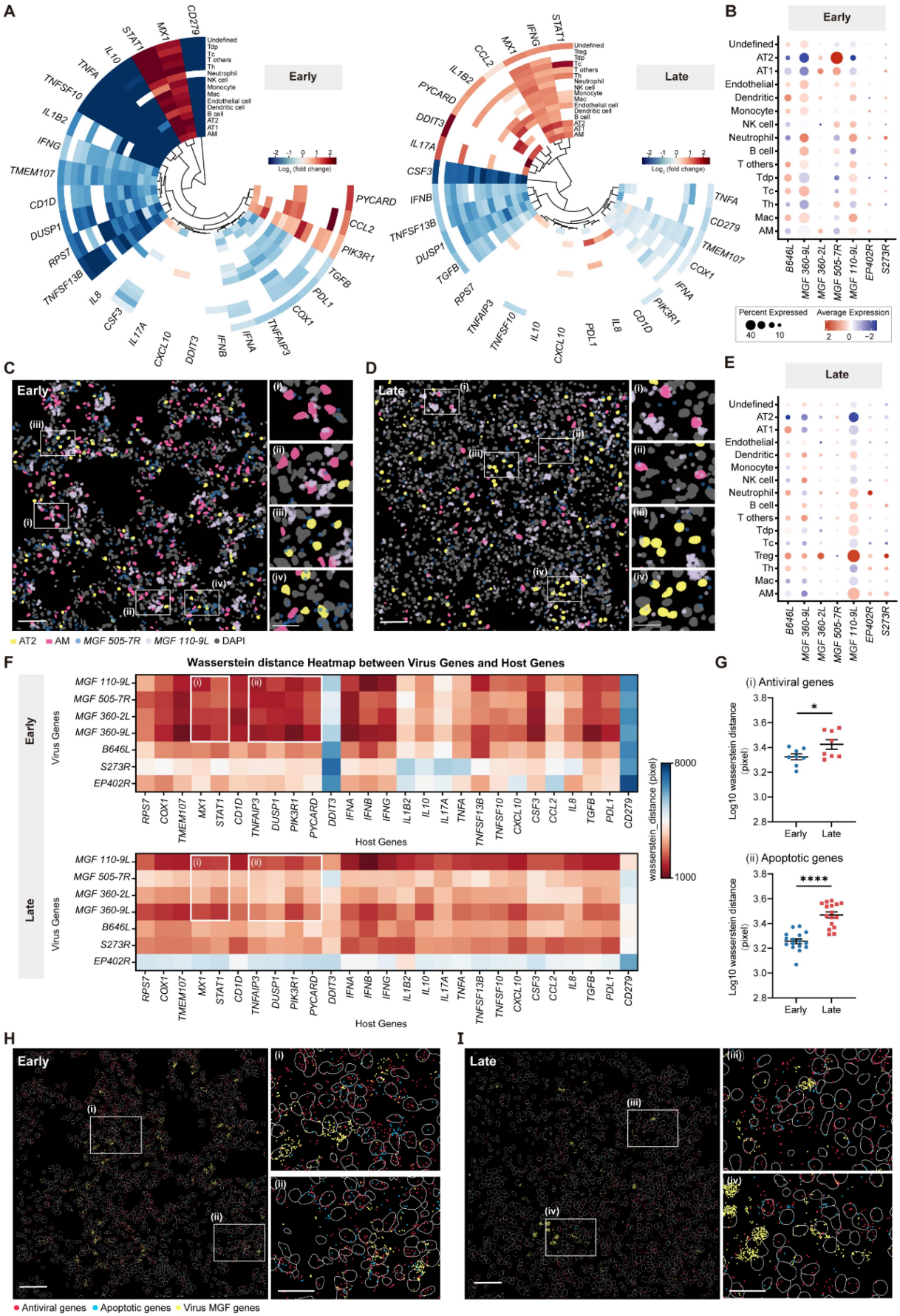

Figure 5. Spatial transcriptomic change of viral and host genes in different types of cells and their correlation. (A) Differential expression of 27 host genes in different cell types at early and late stages of infection compared to controls. Red and blue color

Our findings indicate that ASFV viral signals were also detected in T cells from the lungs of pigs, with a higher frequency of viral signals observed in lung T cells (16–-18%). Additionally, we validated previous research in the spleen and confirmed the presence of ASFV viral signals in T cells. It is important to emphasize that our current study only detected viral signals in T cells and does not infer that these cells are necessarily "actively infected" or producing virus. Therefore, further studies are needed to clarify the specific impact of ASFV on T cells within the immune microenvironment.

Additionally, the proportion of ASFV-infected monocytes in porcine lungs appears lower than that observed in porcine spleens. These observed variations in ASFV infectivity may arise from differences in organ-specific tissue microenvironments. Further studies are needed to clarify the underlying mechanisms of ASFV infection across different immune cell populations. While our spatial transcriptomic analysis detected ASFV infection across all annotated cell types in porcine lungs, quantitative assessment revealed macrophages and alveolar macrophages as the predominant infected populations, excluding undefined cell types. Further, widespread and exacerbated cell apoptosis occurred across all cell types in pig lungs during ASFV infection, with undefined cells dominating apoptotic population. Since our study primarily focuses on immune cell types, various structural cells in the pig lung (such as alveolar fibroblasts, ciliated cells, and capillary cells) have not been classified and are categorized as "undefined cells." This classification is not due to technical limitations but rather the constraints of the current marker panel, which is insufficient to fully annotate these cell types. Future refinement of undefined cell populations through expanded marker panels will characterize the precise identity of the undefined cell types susceptible to ASFV infection and the apoptotic undefined cells upon ASFV infection, providing critical insights into ASFV pathogenesis mechanisms.

Due to the exceptionally high costs associated with conducting ASFV infection experiments in BSL-3 facilities, we selected the minimum scientifically acceptable sample size ($n = 3$ per group). Meanwhile, to accurately represent *in vivo* gene expression, we excluded the deceased pig from the early infection group since post-mortem tissue alterations would compromise the accuracy of gene expression profiling. Although the sample size is limited, the consistent clustering patterns across images from different lung lobes and the relatively small standard deviations of the statistical results suggest that our findings are reasonably reliable. At the same time, expanding the sample size could further strengthen the stability of the conclusions.

Taken together, our study delineated the spatial transcriptomic dynamics of pig lung microenvironment during ASFV infection at single-cell resolution. The *in vivo* transcriptomic dynamics indicated concurrent activation of host immune responses against ASFV and viral-mediated immunosuppression, highlighting the intricate ASFV-host interplay within the lung immune microenvironment. The spatial dynamics of different cell types during ASFV infection will provide new perspectives for understanding the functions and interactions of immune cells during viral infections. Our spatial transcriptomic approach overcomes limitations inherent to antibody-based protein detection. However, the platform only measured transcriptional activity of genes, not protein abundance or post-translational modifications. The spatial gene expression changes in the porcine pulmonary immune microenvironment following ASFV infection require subsequent protein-level validation when corresponding antibodies become available. Nevertheless, our results not only revealed the complexity of the immune microenvironment during ASFV infection but also provided new data and visual evidence for understanding ASFV pathological mechanisms.

Materials and methods

Animals

Animal experiments were carried out in accordance with the guidelines for the care and use of laboratory animals by Research Ethics Committee of Huazhong Agricultural

respectively indicates up- and down- regulation of gene expression. (B) Bubble plot of viral genes expression in different types of cells at early infection stage. (C-D) Expression of *MGF 505-7 R* and *MGF 110-9 L* in AT2 cells and AM cells. The box areas of i-iv are magnified on the right panels. (E) Bubble plot of viral genes expression in different types of cells at late infection stage. (F) Wasserstein distance heatmap between viral genes and host genes. A shorter Wasserstein distance indicates higher expression correlation. White boxes of i and ii respectively highlights the distance relationships of viral MGF genes with host antiviral response-related genes and apoptosis-related genes. (G) Statistical significance of Wasserstein distance for i and ii between early and late infection stage. Statistical significance was measured by Student's t-test (two-tailed). *$p < 0.05$, **$p < 0.0001$. (H-I). Expression of viral MGF genes and host antiviral response-related genes as well as apoptosis-related genes in early (H) and late (I) sample slices of infection. The box areas of i-iv are magnified on the right panels. Scale bars, 50 μm in left panels of C-D and H-I, 20 μm in right panels of C-D and H-I.

University (license no. HZAUSW-2024–0042). All experiments on live manipulation of ASFV and animal infection were conducted in the animal biosafety level 3 (ABSL-3) laboratory of Huazhong Agricultural University approved by the Ministry of Agriculture and Rural Affairs of China. All experimental procedures were designed to minimize animal suffering and were approved by the institutional ethics committee, ensuring compliance with ethical standards for animal research.

Infection

The ASFV SY-1 strain [51], a highly virulent strain, was previously isolated by our laboratory from ASFV infected wild boars in Shennongjia Forest, Hubei Province, China, which was reported by the Ministry of Agriculture and Rural Affairs of China. And ASFV SY-1 strain was preserved in our BSL-3 facility and used for the infection. Twelve healthy piglets (Landrace, 70 days old, bought from Xianning Shentong Animal Husbandry Co., Ltd.) were randomly divided into four groups (3 piglets/group). The piglets were housed in individual pens, with three piglets per pen, under controlled environmental conditions, and were provided with standard feed and ad libitum water. Two groups (early infection group and late infection group) were orally challenged with ASFV SY-1 strain (2×10^2 HAD_{50}), and the other two groups served as controls (early control group and late control group) receiving equivalent volumes of solvent vehicle. Tissues were collected from early infection and control groups at 11 days post infection (dpi), and from late infection and late control groups at 23 dpi. The piglets for this study were free of ASFV, porcine circovirus, and porcine reproductive and respiratory syndrome virus. During 23-day infection period, all challenged piglets were monitored daily for rectal temperature. And oral, nasal, and rectal swab samples were collected from the challenged pigs to measure the viral load.

Tissue slice preparation

Pig lung and spleen tissues were dissected out and fixed in 4% paraformaldehyde (PFA) in PBS for 24 hours (h) at 4°C. Following fixation, tissues were trimmed and dehydrated in gradient ethanol, followed by embedding in paraffin. Subsequently, tissue blocks were cut into 4 μm sections for use.

TUNEL assay

Tissue sections were subjected to TUNEL assay using apoptosis detection kit (YEASEN, 40306ES20) according to the manufacturer's instruction. Fluorescent images were acquired using a Leica TCS SP8 confocal microscope. The TUNEL-positive cells were counted, and the apoptosis index was calculated according to the following formula: (number of apoptotic cells/total number of nuclei) × 100%.

In situ multi-gene mRNA co-detection

Paraffin slices were subjected to a series of pretreatments including dewaxing, rehydration, dehydration, proteinase K treatment, and another dehydration. Subsequently, slices were subjected to *in situ* multi-gene mRNA co-detection via spatial omics method MiP-seq [52], with sequencing probes replaced by detection probes. Through dual-barcode strategy, transcripts of 10 genes can be interrogated for each round detection, and 50 genes will be decoded after five rounds of detection. The sequences for all probes used in this study were listed in Table S1.

Co-detection of P72 protein and marker genes mRNAs

The lung tissue slices were first incubated with mouse anti-P72 antibody (1:100 dilution in 0.3% Triton X-100 + 1% BSA in PBS) overnight at 4°C. After triple washes with 1× PBS, slices were incubated with Alexa Fluor™ 488 labeled goat anti-mouse IgG (Thermo Fisher, A11001, 1:500 dilution) for 1 hour at 37°C. Then slices were washed with 1× PBS and counterstained with DAPI, followed by imaging by fluorescence microscope (Leica, Germany). Subsequently, the slices were subjected to multiplexed *in situ* mRNA co-detection for marker genes of B cells (*CD19*), NK cells (*CD94*), and neutrophils (*MPO*).

Image alignment

Image alignment across five detection rounds was performed by BigWarp function in ImageJ (version 2.9.0, Fiji is Just). The first-round image was designated as the target image, while the subsequent rounds of images served as the moving images. Alignment was achieved by registering the position of cell nuclei stained with DAPI across all imaging rounds. This process involved feature-based registration, utilizing both affine and non-linear transformations to ensure precise spatial correspondence. The accuracy of registration was validated by quantifying the overlap and positional consistency of DAPI-stained nuclei across the aligned images.

Spots calling and decoding

All spots in the images were identified by deep learning model U-FISH (codes available at https://github.com/UFISH-Team/U-FISH) with the intensity threshold set to 0.1. Individual channels were combined to analyze the intensity of dual barcode spots [53]. For each spot, all codes from each round were merged to generate their barcode. Gene decoding was achieved by matching the barcode with the gene codebook (Table S1).

Cell segmentation and genes assignment

Cell segmentation was performed using Cellpose package (version 1.0.2). For cells challenging to segment with Cellpose, manual segmentation was conducted using Napari software (version 0.4.18). After cell segmentation, all cell masks and their corresponding positional information were meticulously obtained [54]. To integrate decoded gene results with cell segmentation outcomes, we employed gene_to_cell function to obtain a single-cell resolution expression matrix with spatial positional information. The expression matrix containing spatial coordinates of genes and a cell mask array representing segmented cells were used as inputs. Genes were initially assigned to cells based on a distance threshold, which determines the maximum distance for the initial assignment, iterating up to a specified maximum number of iterations, with each iteration increasing the distance threshold by a fixed step. The spatial coordinates of genes were used to locate their positions relative to the cell masks, and the nearest cell for each gene spot was computed. The related center coordinates for each gene were calculated and formatted into a string representation. Finally, a DataFrame containing each gene and its assigned cell was created. And the frequency of each gene-cell assignment was calculated to construct the expression matrix, with genes as rows and cells as columns.

Cell-type annotation

Cell types were annotated based on the expression of marker genes by calculating the MGEscore (codes available at https://github.com/wikk-chy/MGEscore). The process began by determining a ranking score for the expression of each marker gene. Gene expression levels were ranked in descending order, with ties assigned the minimum rank. The score for each gene was derived by dividing the maximum rank by the rank of the gene expression in each cell. For each cell type, we identified its specific marker genes and calculated their individual scores. The weighted average score for each cell type was then obtained by averaging these individual scores. To assign cell types, we compared the weighted average scores across all cell types for each cell. A cell was annotated as a specific cell type if its score for that cell type was significantly higher than the scores for other cell types. If no cell type showed a markedly higher score, the cell was classified as "undefined."

Bubble plots of marker genes and viral genes expression were generated using the DotPlot_scCustom function from the R package scCustomize (version 2.1.2). Waterfall plots of cell proportion were generated using the ggplot2 package (version 2.1.2) in R. To analyze cell clustering difference between samples from distinct lung lobes, principal component analysis (PCA) was performed on host genes using RunPCA function in the Seurat (version 5.0.1) package in R, and then Uniform Manifold Approximation and Projection (UMAP) plots were generated using RunUMAP function in Seurat.

Mean hop distance analysis

To analyze mean hop distance between cell clusters, Sopa (available at https://github.com/gustaveroussy/sopa) was utilized [55]. The analysis began by calculating the spatial locations of cells to construct Delaunay graphs, which connected each cell to its nearest neighbors, forming a network of triangles that cover the spatial domain without overlapping edges. To ensure realistic cell-cell interactions, we pruned edges longer than 50 μm. However, for cell clusters with fewer numbers, edges up to 100 μm were selected. Using the pruned Delaunay graph, we calculated the mean hop distance between different cell clusters by determining the number of edges in the shortest path connecting them within the graph. For each pair of cell clusters, the average hop distance was computed by considering all pairwise distances between cells of the two clusters. These mean hop distance values were recorded and analyzed to understand the spatial relationships between different cell clusters. Since cell number can influence the mean distance, we further validated the reliability of our findings by using the sopa.spatial.cell_to_groups function. This function calculates the distance between each cell and all cell types, followed by statistical significance testing.

Statistical analysis

For all statistical analysis on images of pig lungs, 6 images from two lung slices of two pigs in early mock group, 7 images from two lung slices of two pigs in early infection group, 9 images from three lung slices of three pigs in late mock group, and 10 images from three lung slices of three pigs in late infection group

were subjected to comparison. For statistical analysis on pig spleens, 6 images from two spleen slices of two pigs in early infection group and 9 images from three spleen slices of three pigs in late infection group were subjected to differential significance analysis. All image analysis were performed in Python (version 3.7.12). Statistical analysis was performed using R version 4.3.2 and GraphPad Prism 9 statistical software. Data were expressed as mean ± SEM and were analyzed for statistical significance by Student's t-test (two-tailed). Significant differences were considered as follows: $^{*}p < 0.05$, $^{**}p < 0.01$, $^{***}p < 0.001$, and $^{****}p < 0.0001$.

For analysis of overall gene expression change at single-cell resolution, gene expression data for 27 host genes from individual cells in all images of lung slices were normalized and log-transformed to ensure comparability and reduce technical variability. The R package ggpubr (version 0.6.0) was used to create violin plots. To assess the statistical significance of differences in gene expression between sample groups, we employed the Wilcoxon rank-sum test. The significance levels were denoted as follows: $^{*}p < 0.05$, $^{**}p < 0.01$, $^{***}p < 0.001$, and $^{****}p < 0.0001$.

Detailed Description of the materials and methods

Detailed procedures of tissue slice preparation, Hematoxylin-Eosin Staining, *in situ* multi-gene mRNA co-detection, and further bioinformatic analysis (including spatial autocorrelation analysis, viral-load state determination, apoptosis analysis of cell type, Wasserstein metric analysis, and spatial immune microenvironment analysis) are described in supplemental materials. The entire study was conducted between May 2024 and January 2025. [56–58]

Acknowledgements

We thank Z. Hu, Y. Li and C. Shi in the Core Facility at HZAU for technical support in imaging.

Author contributions

CRediT: **Hui Guo:** Data curation, Formal analysis, Methodology, Resources, Visualization, Writing – original draft, Writing – review & editing; **Huaiyuan Cai:** Formal analysis, Resources, Software, Validation, Visualization; **Yu Chen:** Formal analysis, Visualization; **Zhong Zou:** Data curation, Formal analysis, Validation; **Shengjie Yin:** Formal analysis; **Yangyang Xu:** Formal analysis, Resources; **Guiqing Peng:** Supervision; **Meilin Jin:** Resources, Supervision; **Gang Cao:** Project administration, Supervision; **Jinxia Dai:** Funding acquisition, Investigation, Project administration, Supervision, Validation, Writing – original draft, Writing – review & editing.

Funding

This work was supported by the National Key Research and Development Program of China [Grant No. 2021YFD1800100].

Disclosure statement

No potential conflict of interest was reported by the author(s).

Data availability statement

All data generated or analyzed during this study are deposited in Figshare. The original images are available at https://doi.org/10.6084/m9.figshare.28827272 [56]. The datasets for all figures and supplemental figures generated during data analysis, the single-cell resolution expression matrix for genes, and supplemental information (including supplemental methods and materials, supplemental figures with legends, and supplemental table with legends) are available at https://doi.org/10.6084/m9.figshare.28784414 [57].

The source code for the ASFV spatialomics analysis is available on GitHub at https://github.com/wikk-chy/ASFV_spatialomics_analysis under the CC-BY-4.0 License, and archived on Zenodo at https://doi.org/10.5281/zenodo.20121053 [58], also under the CC-BY-4.0 License.

Statement of adherence to arrive guidelines

We followed the Animal Research: Reporting of In Vivo Experiments (ARRIVE) guidelines to ensure transparency and integrity in the design, execution, and reporting of our experiments. We have adhered to ARRIVE guidelines and uploaded a completed checklist as supplementary files.

ORCID

Meilin Jin http://orcid.org/0000-0002-3145-9434
Jinxia Dai http://orcid.org/0000-0001-7060-5185

References

[1] Dixon LK, Stahl K, Jori F, et al. African swine fever epidemiology and control. Annu Rev Anim Biosci. 2020;8(1):221–246. doi: 10.1146/annurev-animal-021419-083741
[2] Sánchez-Cordón PJ, Montoya M, Reis AL, et al. African swine fever: a re-emerging viral disease threatening the global pig industry. Vet J. 2018;233:41–48. doi: 10.1016/j.tvjl.2017.12.025
[3] Das PJ, Sonowal J, Sengar GS, et al. Characterization of an African swine fever virus outbreak in India and comparative analysis of immune genes in infected and surviving crossbreed vs. indigenous Doom pigs. Arch Virol. 2024;169(7):145. doi: 10.1007/s00705-024-06062-y
[4] Salguero FJ. Comparative pathology and pathogenesis of African swine fever infection in swine. Front Vet Sci. 2020;7:282. doi: 10.3389/fvets.2020.00282

[5] Zhou X, Li N, Luo Y, et al. Emergence of African swine fever in China, 2018. Transbound Emerg Dis. 2018;65 (6):1482–1484. doi: 10.1111/tbed.12989
[6] Blome S, Franzke K, Beer M. African swine fever – a review of current knowledge. Virus Res. 2020;287:198099. doi: 10.1016/j.virusres.2020.198099
[7] Fan W, Cao Y, Jiao P, et al. Synergistic effect of the responses of different tissues against African swine fever virus. Transbound Emerg Dis. 2021;69(4): tbed.14283. doi: 10.1111/tbed.14283
[8] Salguero FJ, Sánchez-Cordón PJ, Núñez A, et al. Proinflammatory cytokines induce lymphocyte apoptosis in acute African swine fever infection. J Comp Pathol. 2005;132(4):289–302. doi: 10.1016/j.jcpa.2004.11.004
[9] Ju X, Li F, Li J, et al. Genome-wide transcriptomic analysis of highly virulent African swine fever virus infection reveals complex and unique virus host interaction. Vet Microbiol. 2021;261:109211. doi: 10.1016/j.vetmic.2021.109211
[10] Cackett G, Matelska D, Sýkora M, et al. The African swine fever virus transcriptome. J Virol. 2020;94(9): e00119–20. doi: 10.1128/JVI.00119-20
[11] Zheng Y, Li S, Li S-H, et al. Transcriptome profiling in swine macrophages infected with African swine fever virus at single-cell resolution. Proc Natl Acad Sci USA. 2022;119(19):e2201288119. doi: 10.1073/pnas.2201288119
[12] Gao P, Zhou L, Wu J, et al. Riding apoptotic bodies for cell–cell transmission by African swine fever virus. Proc Natl Acad Sci. 2023;120(48):e2309506120. doi: 10.1073/pnas.2309506120
[13] Jiang B, Li L, Wu Y, et al. Unveiling shared immune responses in porcine alveolar macrophages during ASFV and PRRSV infection using single-cell RNA-seq. Microorganisms. 2024;12(3):563. doi: 10.3390/microorganisms12030563
[14] Lv L, Zhang T, Jia H, et al. Temporally integrated transcriptome analysis reveals ASFV pathology and host response dynamics. Front Immunol. 2022;13 (accessed 11 Oct2023). doi: 10.3389/fimmu.2022.995998
[15] Zhu JJ, Ramanathan P, Bishop EA, et al. Mechanisms of African swine fever virus pathogenesis and immune evasion inferred from gene expression changes in infected swine macrophages. PLOS ONE. 2019;14(11): e0223955. doi: 10.1371/journal.pone.0223955
[16] Au-Yeung N, Mandhana R, Horvath CM. Transcriptional regulation by STAT1 and STAT2 in the interferon JAK-STAT pathway. JAKSTAT. 2013;2 (3):e23931. doi: 10.4161/jkst.23931
[17] Gao S, von der Malsburg A, Paeschke S, et al. Structural basis of oligomerization in the stalk region of dynamin-like MxA. Nature. 2010;465 (7297):502–506. doi: 10.1038/nature08972
[18] Wertz IE, O'Rourke KM, Zhou H, et al. De-ubiquitination and ubiquitin ligase domains of A20 downregulate NF-kappaB signalling. Nature. 2004;430 (7000):694–699. doi: 10.1038/nature02794
[19] Galindo I, Hernáez B, Muñoz-Moreno R, et al. The ATF6 branch of unfolded protein response and apoptosis are activated to promote African swine fever virus infection. Cell Death Dis. 2012;3(7):e341–e341. doi: 10.1038/cddis.2012.81
[20] Zhu Z, Mao R, Liu B, et al. Single-cell profiling of African swine fever virus disease in the pig spleen reveals viral and host dynamics. Proc Natl Acad Sci USA. 2024;121(10):e2312150121. doi: 10.1073/pnas.2312150121
[21] Xu H, Dun S, Gao Y, et al. Tmem107 inhibits EMT and invasion of NSCLC through regulating the hedgehog pathway. Thorac Cancer. 2021;12(1):79–89. doi: 10.1111/1759-7714.13715
[22] Karalyan Z, Voskanyan H, Ter-Pogossyan Z, et al. Il-23/IL-17/G-CSF pathway is associated with granulocyte recruitment to the lung during African swine fever. Vet Immunol Immunopathol. 2016;179:58–62. doi: 10.1016/j.vetimm.2016.08.005
[23] Jenson JS, Childerstone A, Takamatsu H-H, et al. The cellular immune recognition of proteins expressed by an African swine fever virus random genomic library. J Immunol Methods. 2000;242(1–2):33–42. doi: 10.1016/S0022-1759(00)00222-2
[24] Oura CAL, Denyer MS, Takamatsu H, et al. In vivo depletion of CD8+ T lymphocytes abrogates protective immunity to African swine fever virus. J Gen Virol. 2005;86(9):2445–2450. doi: 10.1099/vir.0.81038-0
[25] Zhang K, Yang B, Shen C, et al. MgF360-9L is a major virulence factor associated with the African swine fever virus by antagonizing the JAK/STAT signaling pathway. Mbio. 2022;13(1):e02330–21. doi: 10.1128/mbio.02330-21
[26] Li J, Song J, Kang L, et al. Pmgf505-7r determines pathogenicity of African swine fever virus infection by inhibiting IL-1β and type I IFN production. PLoS Pathog. 2021;17(7):e1009733. doi: 10.1371/journal.ppat.1009733
[27] Ren J, Li D, Zhu G, et al. Deletion of mgf-110-9l gene from African swine fever virus weakens autophagic degradation of tbk1 as a mechanism for enhancing type I interferon production. FASEB J: off Publ Fed Am Soc Exp Biol. 2023;37(6):e22934. doi: 10.1096/fj.202201856R
[28] Rodríguez JM, Yáñez RJ, Almazán F, et al. African swine fever virus encodes a CD2 homolog responsible for the adhesion of erythrocytes to infected cells. Journal of virology. 1993. Available from: https://journals.asm.org/doi/10.1128/jvi.67.9.5312-5320.1993 (accessed 7 Nov2024).
[29] Luo J, Zhang J, Ni J, et al. The African swine fever virus protease pS273R inhibits DNA sensing cGAS-STING pathway by targeting IKKε. Virulence. 2022;13 (1):740–756. doi: 10.1080/21505594.2022.2065962
[30] Chen X, Zheng J, Liu C, et al. Cd1d facilitates African swine fever virus entry into the host cells via clathrin-mediated endocytosis. Emerging Microbes Infections. 2023;12(2):2220575. doi: 10.1080/22221751.2023.2220575
[31] Muir A, Paudyal B, Schmidt S, et al. Single-cell analysis reveals lasting immunological consequences of influenza infection and respiratory immunization in the pig lung. PLoS Pathog. 2024;20(7):e1011910. doi: 10.1371/journal.ppat.1011910

[32] Karimi E, Yu MW, Maritan SM, et al. Single-cell spatial immune landscapes of primary and metastatic brain tumours. Nature. 2023;614(7948):555–563. doi: 10.1038/s41586-022-05680-3
[33] Chambuso R, Meena SS. Single-cell spatial immune profiling for precision immunotherapy in Lynch syndrome. J Natl Cancer Cent. 2025;5(1):3–7. doi: 10.1016/j.jncc.2024.12.002
[34] Zhang L. A high-resolution cell atlas of the domestic pig lung and an online platform for exploring lung single-cell data. J GenetGenomics. 2021;48(5):411–425. doi: 10.1016/j.jgg.2021.03.012
[35] Boussiotis VA. Molecular and biochemical aspects of the PD-1 checkpoint pathway. N Engl J Med. 2016;375(18):1767–1778. doi: 10.1056/NEJMra1514296
[36] Murata T. Human herpesvirus and the immune checkpoint PD-1/PD-L1 pathway: disorders and strategies for survival. Microorganisms. 2021;9(4):778. doi: 10.3390/microorganisms9040778
[37] Zheng X, Nie S, Feng W-H. Regulation of antiviral immune response by African swine fever virus (ASFV). Virol Sin. 2022;37(2):157–167. doi: 10.1016/j.virs.2022.03.006
[38] Liu Y, Zhang X, Qi W, et al. Prevention and control strategies of African swine fever and progress on pig farm repopulation in China. Viruses. 2021;13(12):2552. doi: 10.3390/v13122552
[39] Howey EB, O'Donnell V, de Carvalho Ferreira HC, et al. Pathogenesis of highly virulent African swine fever virus in domestic pigs exposed via intraoropharyngeal, intranasopharyngeal, and intramuscular inoculation, and by direct contact with infected pigs. Virus Res. 2013;178(2):328–339. doi: 10.1016/j.virusres.2013.09.024
[40] Xu Q, Li D, Chen X, et al. In vivo study of inoculation approaches and pathogenicity in African swine fever. Vet Sci. 2024;11(9):403. doi: 10.3390/vetsci11090403
[41] Tian Y, Wang D, He S, et al. Immune cell early activation, apoptotic kinetic, and T-cell functional impairment in domestic pigs after ASFV CADC_HN09 strain infection. Front Microbiol. 2024;15:15. doi: 10.3389/fmicb.2024.1328177
[42] Machuka EM, Juma J, Muigai AWT, et al. Transcriptome profile of spleen tissues from locally-adapted Kenyan pigs (Sus scrofa) experimentally infected with three varying doses of a highly virulent African swine fever virus genotype IX isolate: kEN12/Busia.1 (KEN-1033). BMC Genomics. 2022;23(1):522. doi: 10.1186/s12864-022-08754-8
[43] Zhang D, Hao Y, Yang X, et al. Asfv infection induces macrophage necroptosis and releases proinflammatory cytokine by ZBP1-RIPK3-MLKL necrosome activation. Front Microbiol. 2024;15:15. doi: 10.3389/fmicb.2024.1419615
[44] Jeon S, Rowe AM, Carroll KL, et al. Pd-l1/B7-h1 inhibits viral clearance by macrophages in HSV-1–infected corneas. J Immunol. 2018;200(11):3711–3719. doi: 10.4049/jimmunol.1700417
[45] Deb R, Sengar GS, Sonowal J, et al. Transcriptome signatures of host tissue infected with African swine fever virus reveal differential expression of associated oncogenes. Arch Virol. 2024;169(3):54. doi: 10.1007/s00705-023-05959-4
[46] Dalskov L, Gad HH, Hartmann R. Viral recognition and the antiviral interferon response. Embo J. 2023;42(14):e112907. doi: 10.15252/embj.2022112907
[47] Turner MD, Nedjai B, Hurst T, et al. Cytokines and chemokines: at the crossroads of cell signalling and inflammatory disease. Biochim Biophys Acta (BBA) - Mol Cell Res. 2014;1843(11):2563–2582. doi: 10.1016/j.bbamcr.2014.05.014
[48] Oh S-I, Sheet S, Bui VN, et al. Transcriptome profiles of organ tissues from pigs experimentally infected with African swine fever virus in early phase of infection. Emerging Microbes Infections. 2024;13(1):2366406. doi: 10.1080/22221751.2024.2366406
[49] Kim TH, Lee HK. Differential roles of lung dendritic cell subsets against respiratory virus infection. Immune Netw. 2014;14(3):128–137. doi: 10.4110/in.2014.14.3.128
[50] Liu J, Zhang X, Cheng Y, et al. Dendritic cell migration in inflammation and immunity. Cell Mol Immunol. 2021;18(11):2461–2471. doi: 10.1038/s41423-021-00726-4
[51] Lv C, Yang J, Zhao L, et al. Infection characteristics and transcriptomics of African swine fever virus in Bama minipigs. Microbiol Spectr. 2022;10(6):e03834–22. doi: 10.1128/spectrum.03834-22
[52] Wu X. Spatial multi-omics at subcellular resolution via high-throughput in situ pairwise sequencing. Nat Biomed Eng. 2024;8(7): 872–889. doi: 10.1038/s41551-024-01205-7
[53] Xu W, Cai H, Zhang Q, et al. U-FISH: a universal deep learning approach for accurate FISH spot detection across diverse datasets. Genome Biol. 2025;26(1):261. doi: 10.1186/s13059-025-03736-x
[54] Stringer C, Wang T, Michaelos M, et al. Cellpose: a generalist algorithm for cellular segmentation. Nat Methods. 2021;18(1):100–106. doi: 10.1038/s41592-020-01018-x
[55] Blampey Q, Mulder K, Gardet M, et al. Sopa: a technology-invariant pipeline for analyses of image-based spatial omics. Nat Commun. 2024;15(1):4981. doi: 10.1038/s41467-024-48981-z
[56] Guo H, Cai HY, Chen Y, et al. Single-cell spatial immune landscape of ASFV-infected porcine lung microenvironment. Figshare. 2025. Dataset. doi: 10.6084/m9.figshare.28827272.v3
[57] Guo H, Cai HY, Chen Y, et al. Single-cell spatial immune landscape of ASFV-infected porcine lung microenvironment. Dataset. 2025. doi: 10.6084/m9.figshare.28784414
[58] Hy C. Wikk-chy/asfv_spatialomics_analysis: single-cell spatial immune landscape of ASFV-infected porcine lung microenvironment. Zenodo. 2026. doi: 10.5281/zenodo.20121053